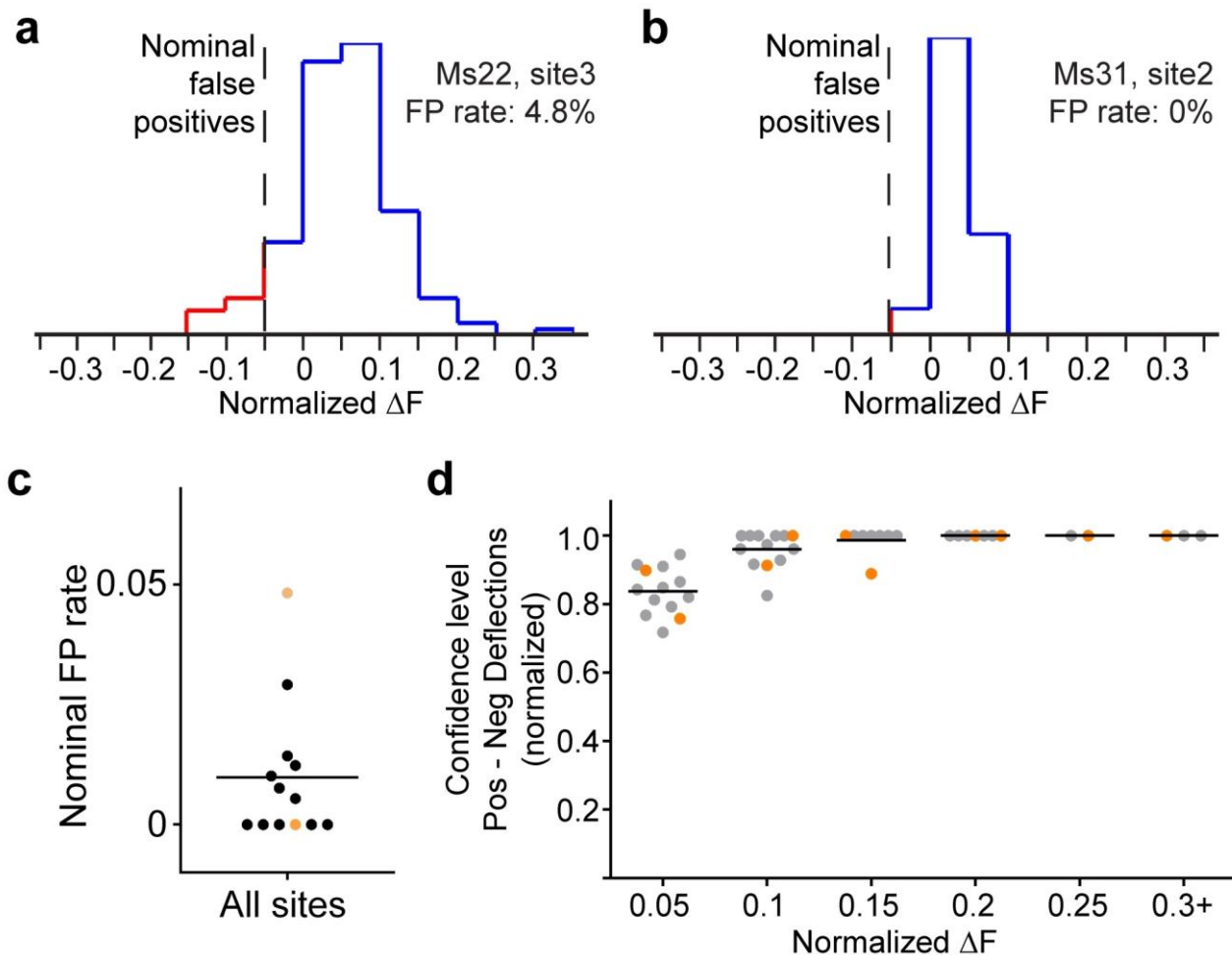


Supplementary Figure 1

### Trial structure for go/no-go behavior

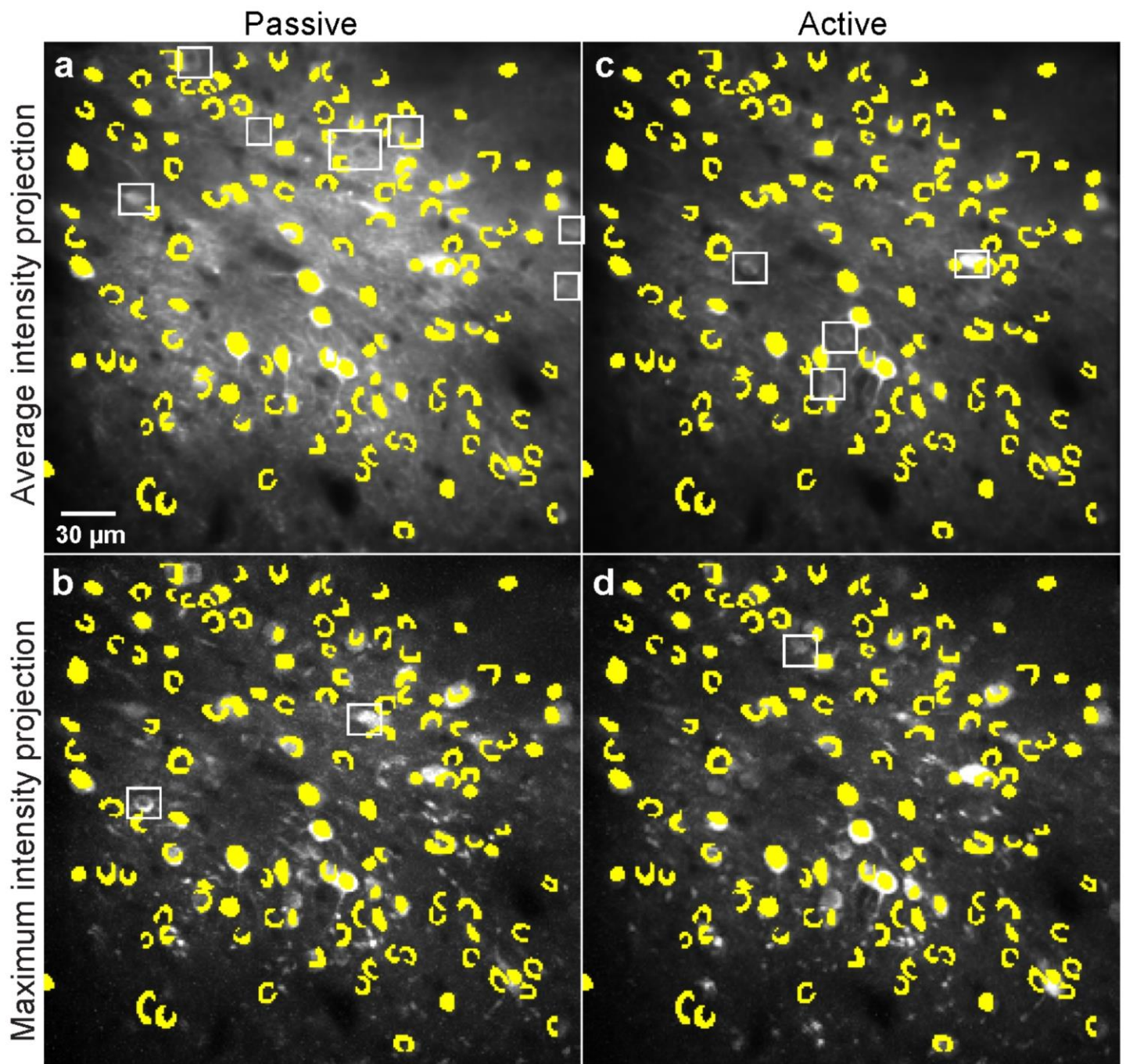
**a**, Overall timeline of experiments. Day 1: A1 mapping, injection of AAV1-SYN-GCaMP6s, cranial window and headpost implantation. Water restriction typically occurred ~7-10 days before initial training. Day 14-21: baseline imaging session to select the target and foil tones. Days 15-30: animal training. Day 20+: imaging session in trained animals. Variability in timeline in terms of start dates for each phase was largely attributable to GCaMP6s expression timing and behavioral learning trajectory. **b**, Normalized lick rate for all animals in all sessions in **Figure 1**, for hit correct trials to the target tone. Thin lines, individual sessions ( $n=5$  mice, 11 sessions); thick line, average performance. **c**, Normalized lick rate for foil tones (correct reject trials). **d**, Performance on go/no-go task over sessions for 11 animals ( $d' = z(\text{hit rate}) - z(\text{false alarm rate})$ ). Dashed line indicates  $d'$  of 1.75, criterion for considering animals fully trained on the task.



**Supplementary Figure 2**

**Identification of false positives due to lick-related brain motion**

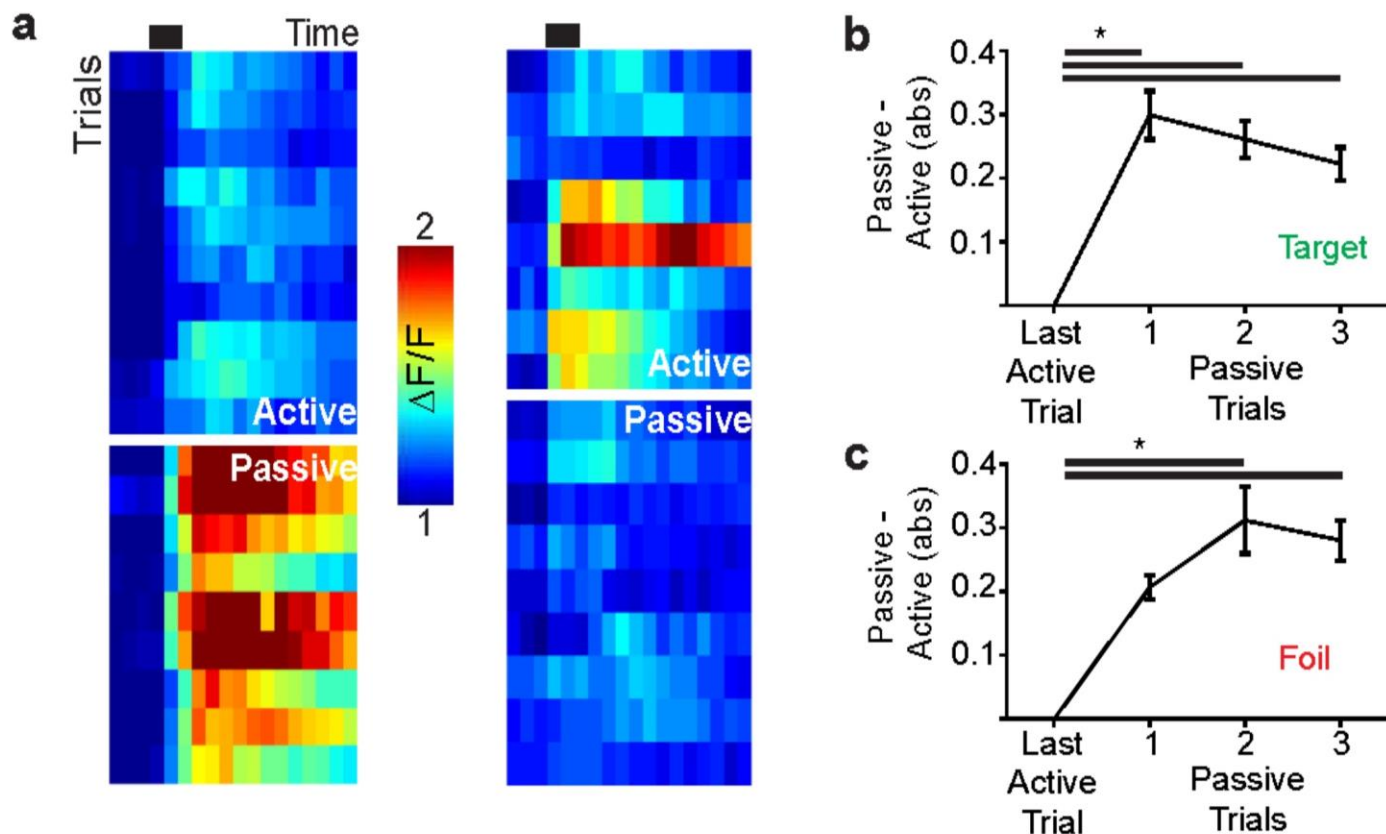
**a**, Histogram of normalized tone-evoked response for one example mouse (animal Ms22). Lick-related brain motion should produce both positive and negative deflections in fluorescence. We calculated the nominal false positive rate as the percent of negative deflections greater than 5%. Vertical dashed line indicates false positive rate. Each animal used in this study had nominal false positive rates below 5% (i.e., 95% likely that positive deflections are not due to licking). **b**, Histogram of normalized responses for another mouse (animal Ms31). **c**, Scatter plot of the nominal false positive rate for all sites in all animals from **Figure 2a-d**. Orange dots are example sites in **a**, **b**. **d**, Confidence level (positive-negative deflection rate) at each normalized  $\Delta F$  value. Even for small changes in fluorescence ( $<0.05$ ), the probability of lick-related brain motion driving the signals is only  $<15\%$ . Orange dots are example sites in **a**, **b**.



**Supplementary Figure 3**

**Matching of neurons between active and passive context**

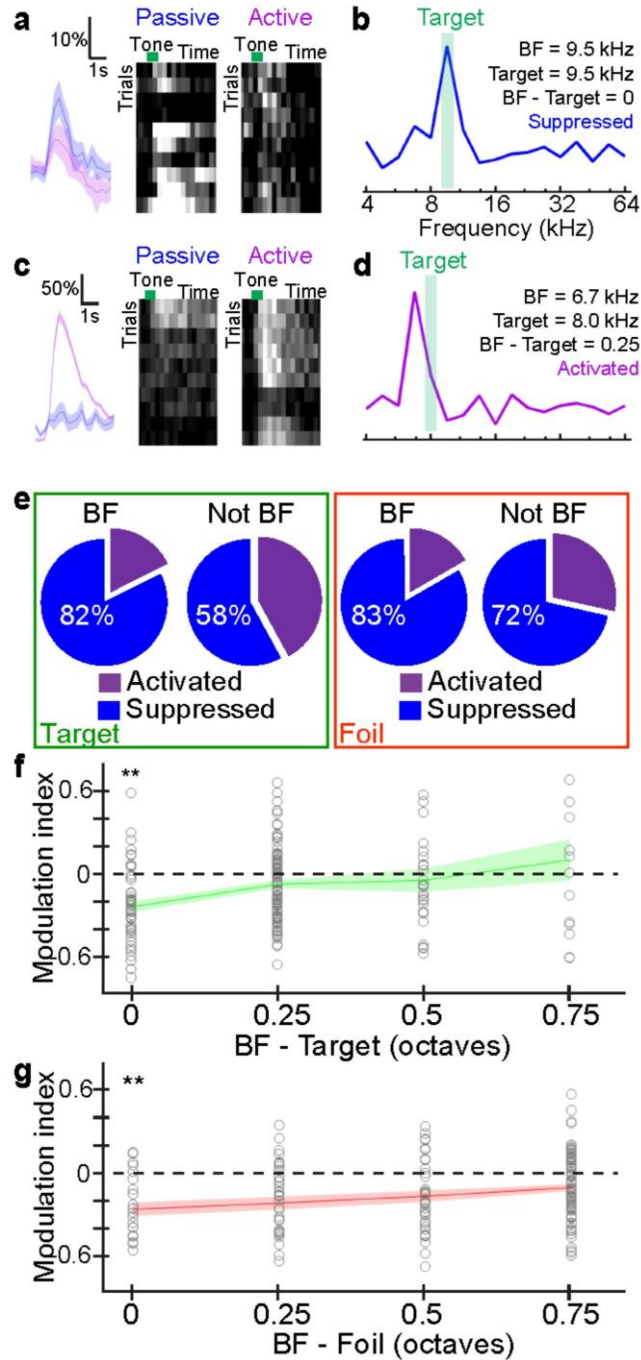
**a,c** Average intensity projection of a single field-of-view in the passive (**a**) and active (**c**) contexts. **b,d**, maximum intensity projections for passive (**b**) and active (**d**) contexts. Yellow cells showed up in both contexts, while white boxes denote cells that were identified in one context but not the other and were excluded from the analysis.



Supplementary Figure 4

#### Rapid switching of neuronal activity after changing contexts

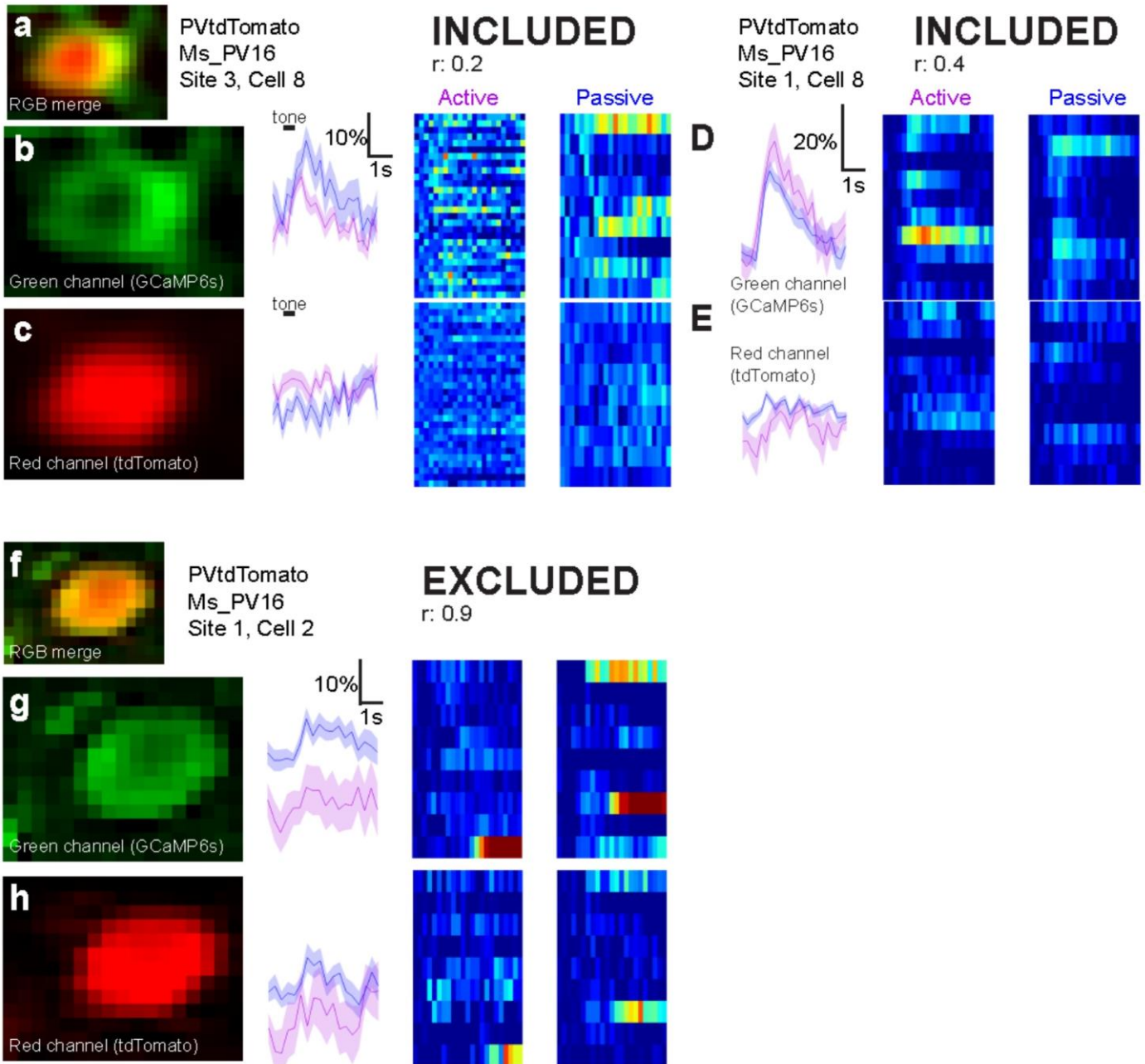
**a**, Heatmap showing trial-by-trial change in calcium response with the transition point (black bar) indicating when the context was switched (~60-90s). Left example shows a "passive-preferring" neuron immediately increasing the tone-evoked calcium response and the right example shows an "active-preferring" neuron with the opposite profile. **b**, Summary of neurons during contextual switching for the target tone. Data is plotted as the absolute change relative to the final active trial ( $n=148$  cells, ANOVA with Tukey's post-hoc). \*,  $p<0.05$ . **c**, as in **b** but measuring responses to the foil tone. For the foil tone, the difference was significant by the second passive trial ( $n=134$  cells, ANOVA with Tukey's post-hoc). \*,  $p<0.05$ .



Supplementary Figure 5

**Task-related suppression was strongest for neurons with best frequencies close to targets or foils**

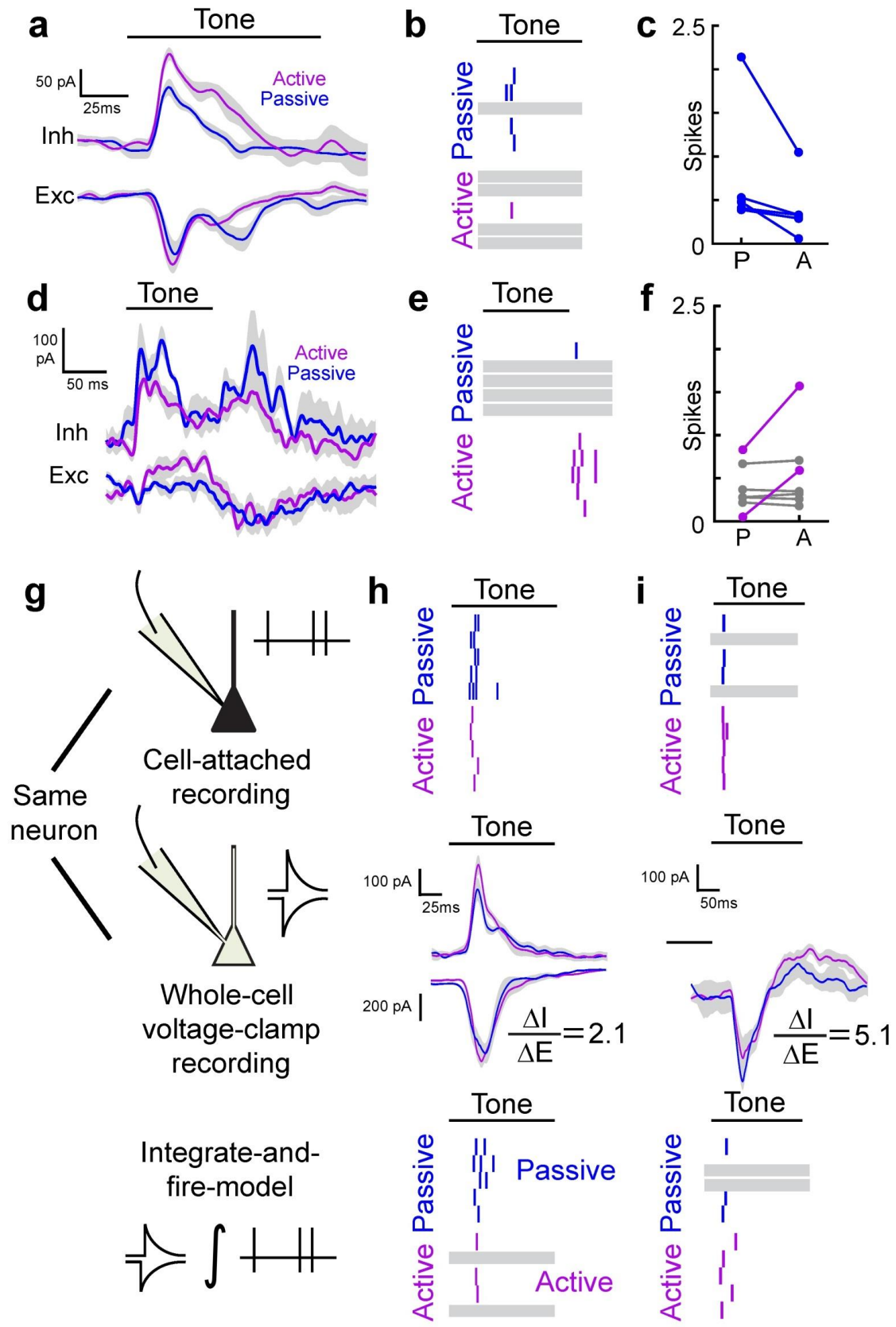
**a**, Example neuron with best frequency (BF) close to target tone. Note significant suppression in active context. **b**, Passive frequency tuning curve for neuron in **a** (500 ms tones, 70 dB SPL, 0.25 octave spacing). Note peak at target frequency. **c**, Example neuron where target tone was 0.25 octaves from BF. This neuron selectively responded during the active context. **d**, Passive frequency tuning curve of neuron in **c**. **e**, Activation and suppression for targets and foils. Note significantly higher suppression at BF (target: 82% suppressed; foil: 83% suppressed) vs not BF (target: 58% suppressed; foil: 72% suppressed,  $p < 0.01$ , Fisher's exact test). **f**, Context modulation (y-axis, negative values indicate suppression, positive values indicate activation) as function of BF relative to target tone (in octaves). Suppression is greatest when target tone is BF (BF-target=0,  $p < 0.002$  versus not BF). **g**, as in **f** but measuring responses to foil tone.



**Supplementary Figure 6**

**Motion artifact exclusion for imaging sessions with tdTomato structural marker**

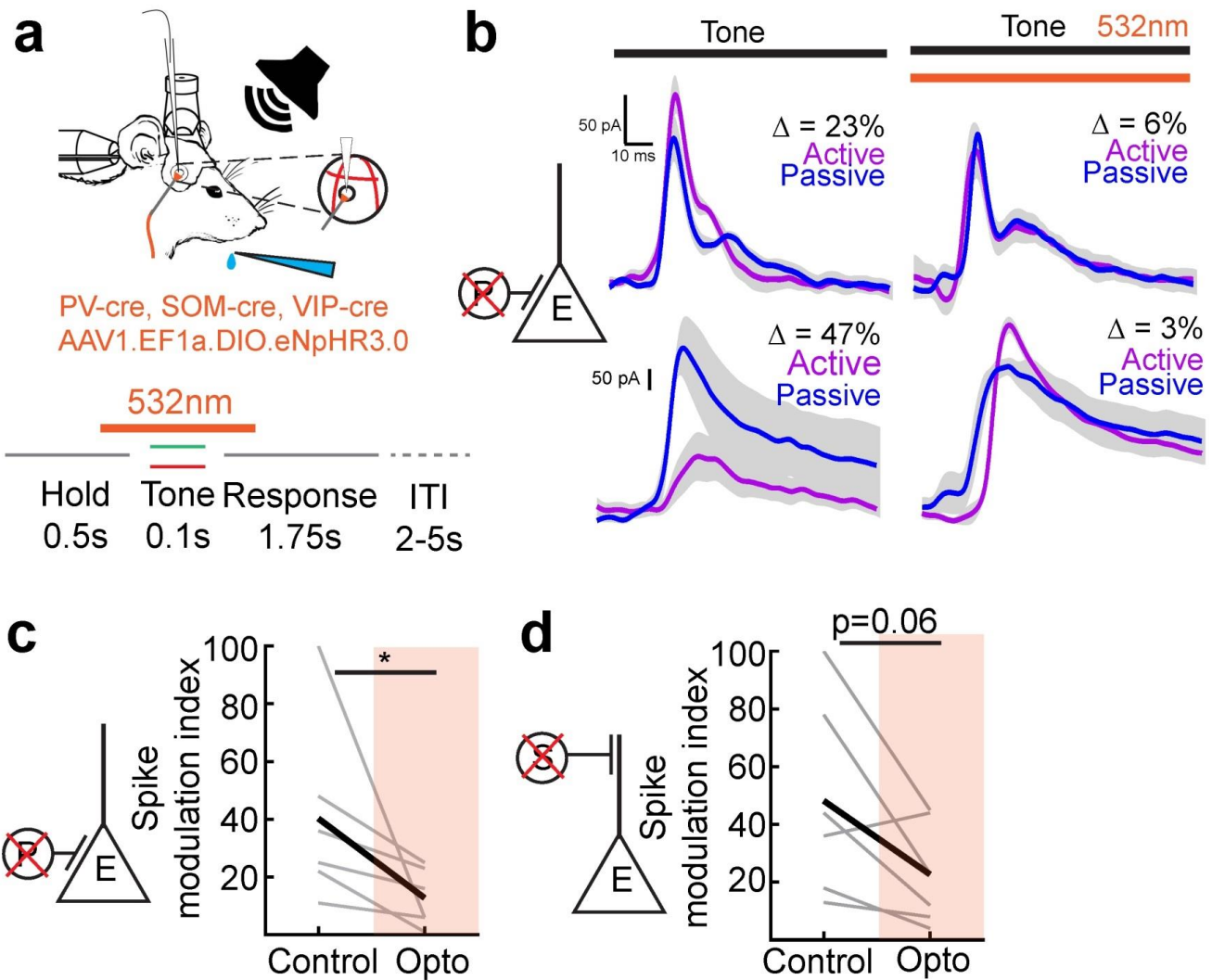
**a**, RGB merge image of a PV+ interneuron (green, GCaMP6s; red, tdTomato). **b**, Green channel image and associated tone-evoked epoch in the active and passive contexts, showing large tone-evoked response. **c**, Red channel image of same neuron and associated tone-evoked epoch, showing lack of response. The cross correlation of these two signals for this neuron was low ( $r: 0.2$ ), and so this neuron was included in the analysis. **d**, Green channel from another example neuron included in the analysis. **e**, Red channel of the cell in **d** (cross-correlation coefficient  $r: 0.4$ ). **f**, RGB merge image of a PV+ interneuron that was excluded. **g**, Green channel image and associated tone-evoked epoch in the active and passive contexts. **h**, Red channel image and associated tone-evoked epoch. Note the high correlation between the red and green channels ( $r: 0.9$ ) even after bleedthrough correction with linear spectral unmixing.



## Supplementary Figure 7

### Spiking model based on synaptic conductances recovers contextual modulation

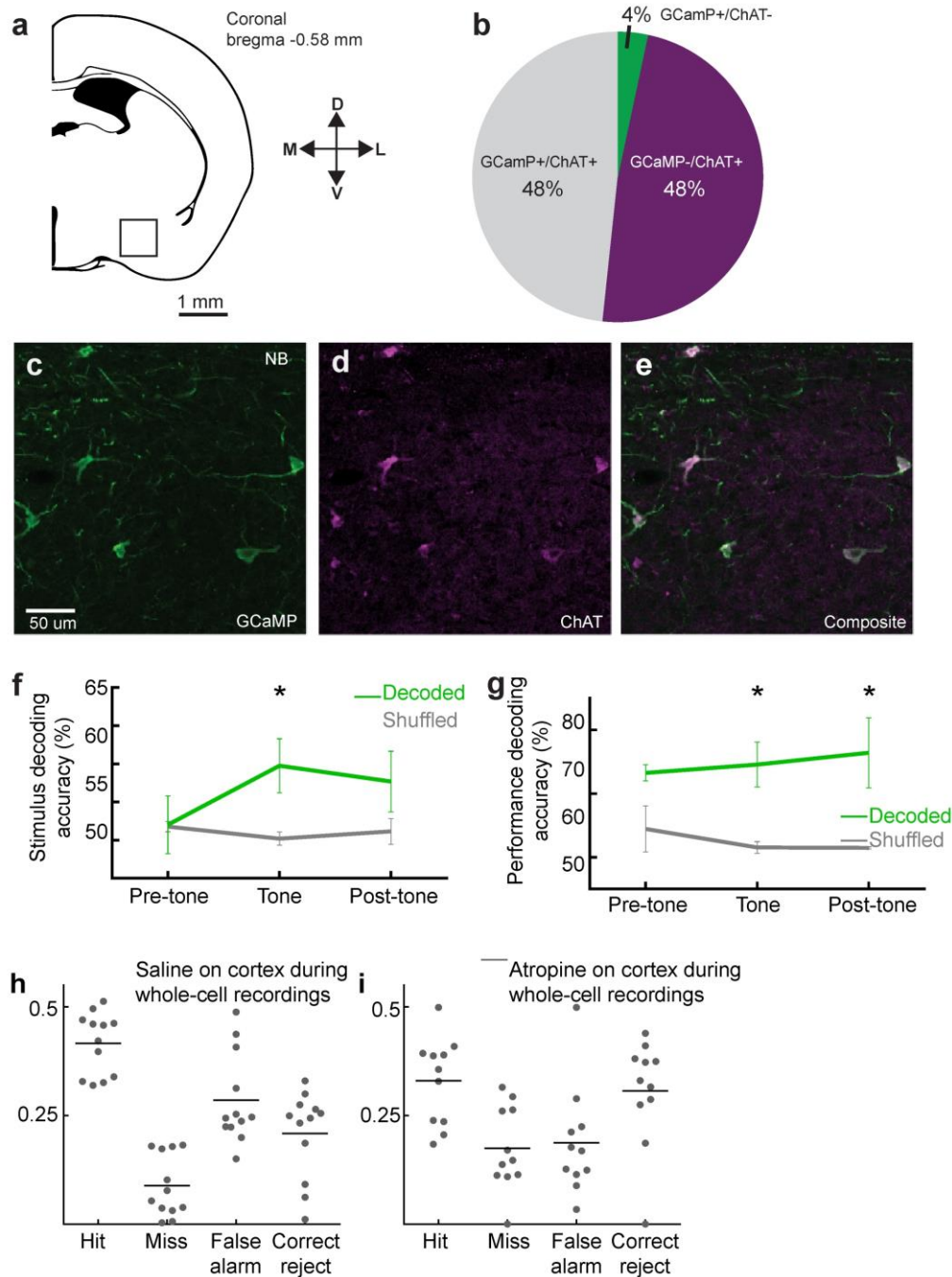
**a**, Example neuron (real recording) showing increased inhibition during the active context. **b**, Results of integrate-and-fire model neuron showing 5 trials of spikes from currents of cell in **a** for the passive (top) and active (bottom) contexts. **c**, Summary of simulations for five neurons with statistically significant suppression ( $n=5$  neurons showing suppression,  $p<0.01$ , two-sided Wilcoxon rank sum test for active versus passive context). **d**, A different example neuron showing decreased inhibition during the active context. **e**, Results of integrate-and-fire model neuron showing 5 trials of spikes from currents of cell in **d** for the passive (top) and active (bottom) contexts. Please note this is likely an off-responding neuron. **f**, Only two neurons exhibited significant activation ( $n=2$  neurons showing activation,  $p<0.01$ , two-sided Wilcoxon rank sum test). Five neurons had no significant difference between contexts ( $n=5$  cells,  $0.36\pm 0.09$  spikes, active context,  $0.36\pm 0.08$  spikes, passive context, average  $p$ -value=0.41, gray lines). **g**, Cell-attached spikes were recorded (top) and then after breaking into the cell, IPSCs and EPSCs were measured (middle). We then put the measured IPSCs and EPSCs through the integrate-and-fire model and predicted spikes and compared that to the experimentally measured spikes. **h**, Cell-attached spike recordings show that this cell is suppressed (-45%) in the active context (top, passive: 17.0 Hz, 0% failure rate (failure = no tone-evoked spike); active: 9.3 Hz, 0% failure rate;  $p<0.01$ , Student's two-tailed paired t-test). Synaptic measurements demonstrate that IPSCs are higher in the active context, more than the corresponding change in EPSCs (middle,  $\Delta\text{IPSC}/\Delta\text{EPSC} = 2.1$ ). Predicting spikes based on the IPSCs and EPSCs show similar levels of suppression (-62%) compared to the experimentally measured active context suppression (bottom, model passive: 11.5 Hz; model active: 4.4 Hz). **i**, Cell-attached spike recordings show that this cell shows a 10% increase in activity in the active context (top, passive: 10.0 Hz, 20% failure rate; active: 11.0 Hz, 0% failure rate;  $p<0.01$ , Student's two-tailed paired t-test). Synaptic measurements demonstrate that IPSCs are lower in the active context, more than the corresponding change in EPSCs (middle,  $\Delta\text{IPSC}/\Delta\text{EPSC} = 5.1$ ). Predicting spikes based on the IPSCs and EPSCs showed similar levels of activation (+6%) compared to the experimentally measured results (bottom, model passive: 6.7 Hz, model active: 7.1 Hz).



Supplementary Figure 8

#### Optical suppression of PV+ and SOM+ interneurons

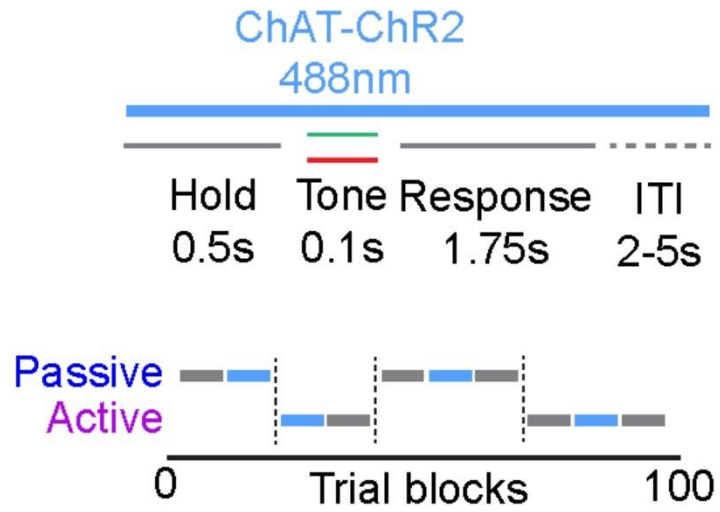
**a**, Experimental paradigm. **b**, Two example cells with whole-cell voltage clamp recording showing loss of context-dependent changes in IPSCs when PV+ interneurons were suppressed. **c**, Optical suppression of PV+ interneurons reduced context-dependent changes in pyramidal spiking. Summary of cell-attached recordings ( $n=5$  neurons in 3 mice, Spike modulation index (control):  $40.3 \pm 13.0\%$ , Spike modulation index (opto):  $12.8 \pm 4.1\%$ ,  $p < 0.05$ , Student's paired two-tailed t-test). **d**, Inactivation of SOM+ interneurons also reduced the context dependent spiking of layer 2/3 pyramidal neurons ( $n=5$  neurons,  $p=0.06$ , Student's paired two-tailed t-test).



**Supplementary Figure 9**

**Effect of atropine on behavioral performance and ChAT histology**

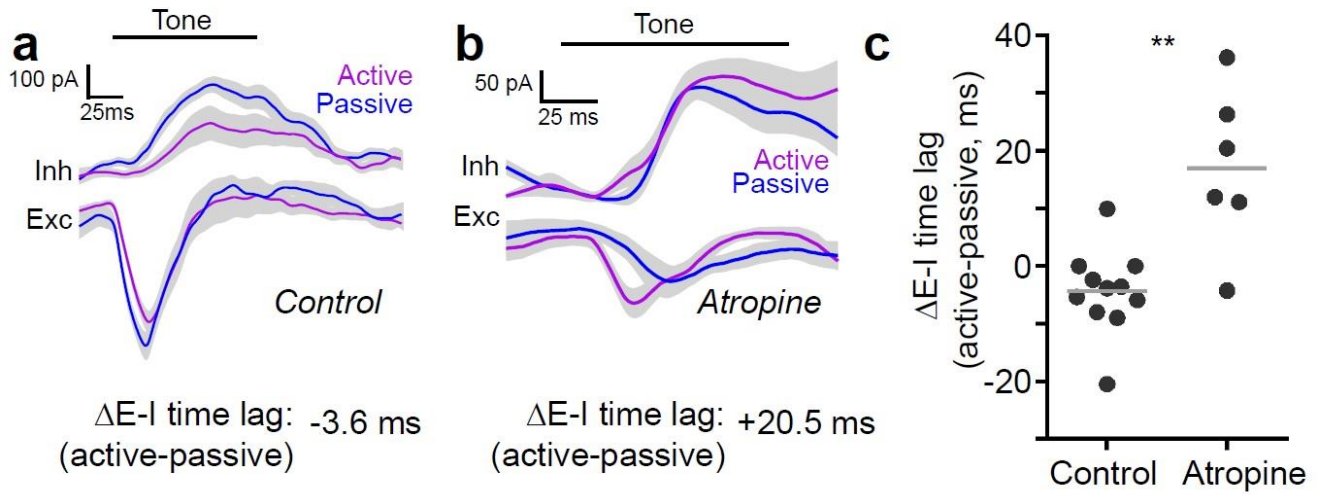
**a**, Coronal slice schematic; black square, area of AAV1-Syn-FLEX-GCaMP6s injection in ChAT-Cre mice into basal forebrain (AP: -0.5 mm from bregma, ML: 1.8 mm on right side, DV: 4.5 mm from surface). **b**, Proportions of GCaMP+/ChAT-, GCaMP+/ChAT+ and GCaMP-/ChAT+ cells ( $n=3$  mice, 15 images, 174 cells). **c**, GCaMP6s expression in nucleus basalis. **d**, ChAT immunohistochemistry in same region. **e**, Overlay showing co-localization of GCaMP6s, ChAT. **f**, Decoding stimulus based on cholinergic terminal activity is effective only during tone period (stimulus: pre-tone,  $p=0.95$ ; tone,  $p=0.04$ ; post-tone,  $p=0.18$ ; Student's t-test). **g**, Decoding action (i.e., licking or no licking) could be predicted by cholinergic terminals even before the tone (pre-tone,  $p=0.06$ ; tone,  $p=0.01$ ; post-tone,  $p=0.04$ ; Student's t-test). **h**, Behavioral outcomes with saline applied to auditory cortex. **i**, Behavior with atropine applied to auditory cortex.



**Supplementary Figure 10**

**Experimental design where blue light tonically illuminates the cortex in a block-based design**

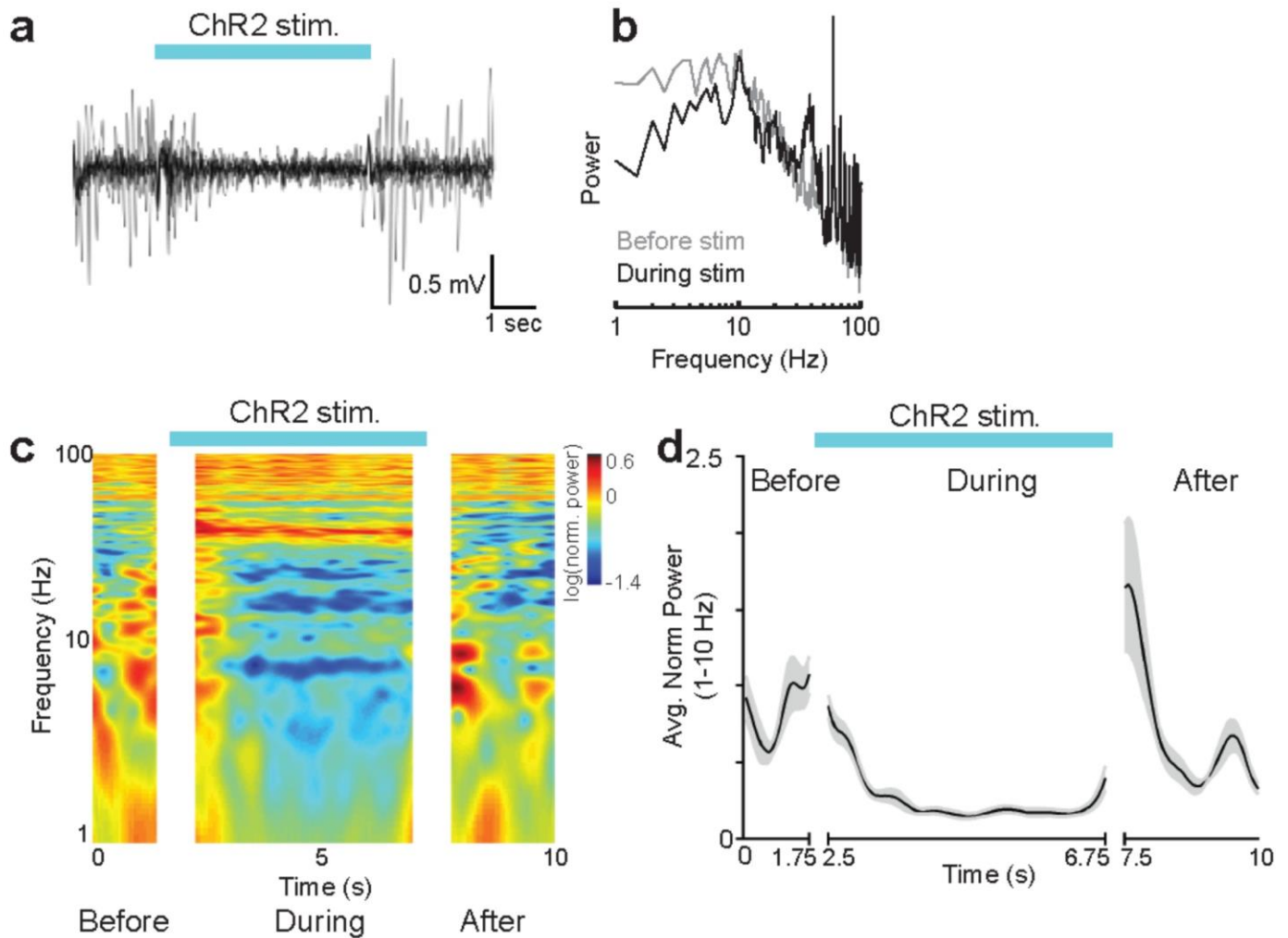
These experiments were performed in fully trained mice.



### Supplementary Figure 11

#### Cholinergic control of inhibition during context-switching

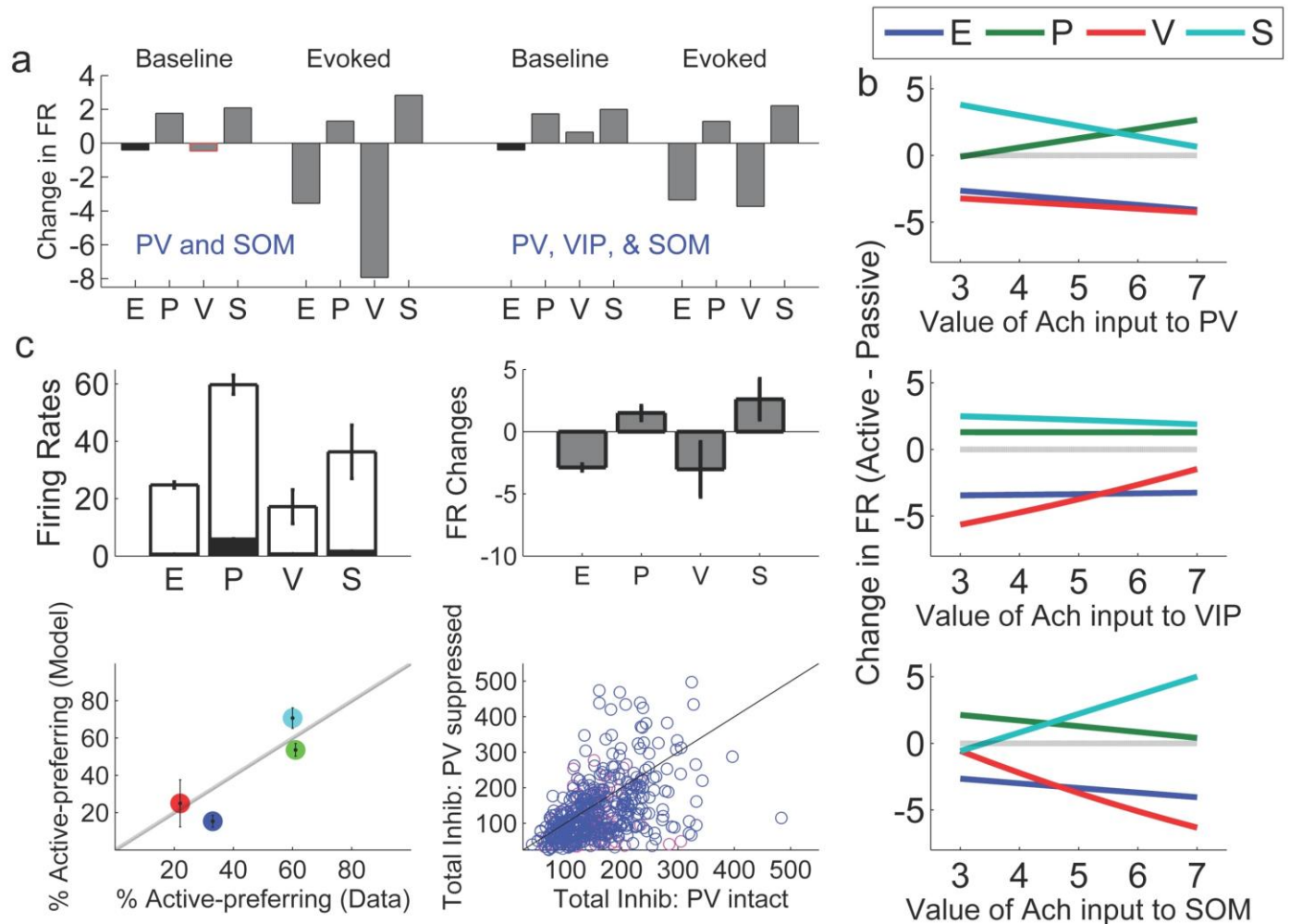
**a**, Example neuron in saline showing that the time lag between excitation and inhibition is smaller in the active context relative to the time lag in the passive context ( $\Delta E-I$  time lag:  $-3.6$  ms, i.e., inhibition and excitation are 3.6 ms closer together in the active context). **b**, Example neuron in atropine showing an increase in the time lag between excitation and inhibition ( $\Delta E-I$  time lag: 20.5 ms). **c**, Summary of the change in time lag of synaptic inputs in the control and atropine conditions (saline:  $n=12$  neurons,  $\Delta E-I$  time lag  $-4.4 \pm 2.2$  ms; atropine:  $n=7$  neurons,  $\Delta E-I$  time lag  $17.0 \pm 5.7$  ms,  $p < 0.05$ , Student's paired two-tailed t-test).



**Supplementary Figure 12**

**Optogenetic activation of cholinergic fibers in mouse auditory cortex**

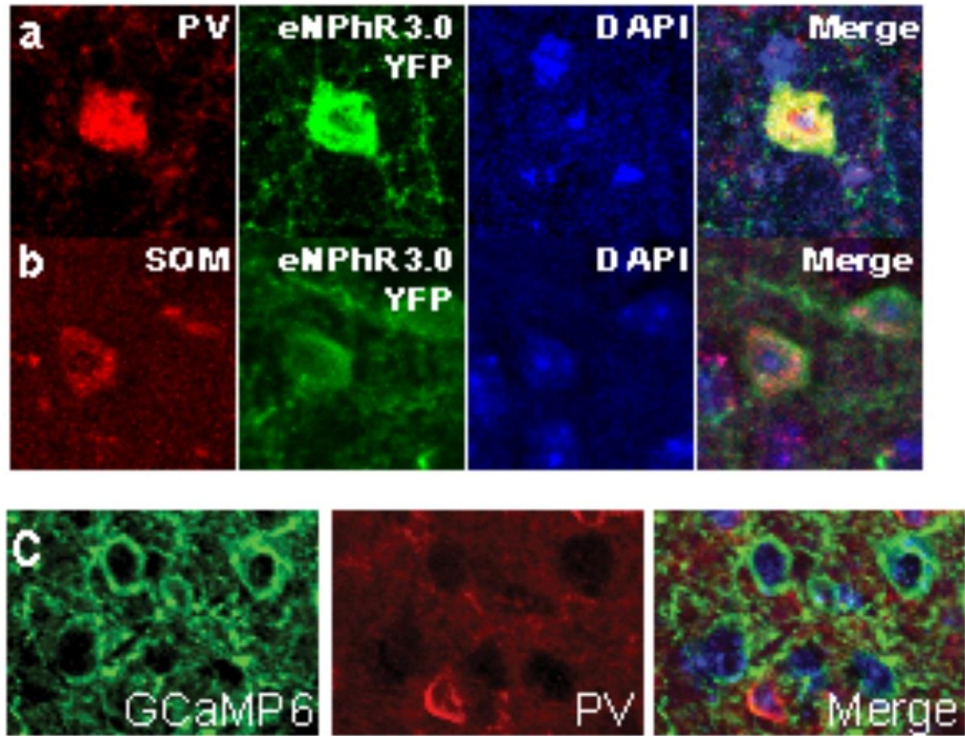
**a**, Overlay of LFP traces from 10 trials showing effect of optical stimulation. Blue bar: 5 sec period of laser stimulation. **b**, Amplitude spectra during 2 s before (gray) and during (black) stimulation, averaged from 10 optical stimulation trials. **c**, LFP spectrogram averaged from 10 trials, normalized by average power during pre-stimulation period. Blue bar: laser stimulation. **d**, Low-frequency power (1-10 Hz) was significantly decreased by optical stimulation of cholinergic fibers in auditory cortex (Pre-stim vs. During-stim,  $P < 0.01$ , Wilcoxon sign-rank test). Blue bar: laser stimulation. Interruptions in axes in **d,e** are periods of light-induced artifact on tungsten electrode.



**Supplementary Figure 13**

**Additional model results and tests for robustness**

**a**, Changes in firing rates in the 4-unit model (active context minus passive context), when ACh is modeled as input to PV and SOM cells alone (left) or all three inhibitory subtypes (right). PV & SOM alone can recapitulate the changes in evoked rates but causes VIP to decrease during baseline, pre-tone firing. Activating all three subtypes causes correct changes in evoked rates and correctly increases VIP in baseline rates. Excitatory baseline firing is slightly reduced. **b**, Robustness of firing rate changes to uneven strengths of ACh across inhibitory cell types. Each panel shows the effects of changing  $I^A$  to the given subtype while holding it constant at 5 for the other 2 subtypes. The directional changes in firing rates remain correct for all 4 cell types over wide ranges. **c**, Multi-unit model results are similar to 4-unit model. Upper-left shows average baseline (black) and evoked (white) firing rates in the passive context. Upper-right: average changes in firing rates (active-passive). Lower-left: Diversity of firing rate changes in each cell type population represented as the percentage of active-prefering cells (data versus model). Color scheme as in **b**. Errorbars represent  $\pm 1$  std from 20 network realizations. Lower-right: Tests of optical suppression experiments. Inactivation of PV cells in the model (cells shown here from a single example network) shifts total inhibition (sum of inhibitory inputs in Passive and Active conditions) downward on average but some cells have increased inhibition similar to observed results (**Supplementary Fig. 8b**). The direction of inhibition changes does not depend on whether the cell was active (magenta) or passive (blue) -preferring before inactivation.



**Supplementary Figure 14**

**Histology**

**a**, We confirmed that our optical suppression of PV+ neurons was selective (PV-cre mice injected with AAV1.EF1a.DIO.eNpHR3.0) by co-staining neurons using an anti-PV antibody (red) and one for GFP to recognize the eNpHR3.0-YFP (green). DAPI nuclear staining is in blue. **b**, Similar co-staining for somatostatin in SOM-cre mice injected with AAV1.EF1a.DIO.eNpHR3.0. **c**, CaMK2-GCaMP6f is largely excluded from PV+ interneurons, the largest inhibitory subtype in the cortex (93.3±3.3% of GCaMP6+ neurons do not exhibit detectable staining for PV, n=70 GCaMP6+ neurons in 2 mice).